1 **RESEARCH ARTICLE**

2 **MATERIALS SCIENCE**

3 **Non-hygroscopic ionogel-based humidity-insensitive iontronic sensor arrays for**

4 **intra-articular pressure sensing**

5 Junli Shi[1,†], Sai Xie[1,†], Zhiguang Liu[1], Minkun Cai[1] and Chuan Fei Guo[1,2,*]

6 [1]Department of Materials Science and Engineering, Southern University of Science and

7 Technology, Shenzhen 518055, China;

8 [2]Guangdong Provincial Key Laboratory of Functional Oxide Materials and Devices,

9 Southern University of Science and Technology, Shenzhen 518055, China

10 ***Corresponding author.** E-mail: <u>guocf@sustech.edu.cn</u>

11 [†]Equally contributed to this work.

12

13 **ABSTRACT**

14 Implanted pressure sensors can provide pressure information to assess localized health

15 conditions of specific tissues or organs, such as the intra-articular pressure within knee

16 joints. However, the prerequisites for implanted sensors pose greater challenges than

17 those for wearables or for robots: aside from biocompatibility and tissue-like softness,

18 they must also exhibit humidity-insensitivity and high pressure-resolution across a broad

19 pressure spectrum. Iontronic sensors can provide superior sensing properties, but they

20 undergo property degradation in wet environments due to the hygroscopic nature of their

21 active component, ionogels. Herein, we introduce a humidity-insensitive iontronic sensor

22 array based on a hydrophobic and tough ionogel polymerized in a hydrophobicity

23 transition yielding two hydrophobic phases: a soft liquid-rich phase enhancing ionic

24 conductivity and ductility, and a stiff polymer-rich phase contributing to superior

25 toughness. We demonstrate the *in vivo* implantation of these sensor arrays to monitor

26 real-time intra-articular pressure distribution in a sheep model, while assessing knee

27 flexion with angular resolution of 0.1° and level pressure resolution of 0.1%. We

28 anticipate that this sensor array will find applications in various orthopedic surgeries and

29 implantable medical devices.

30 **Keywords**: iontronic pressure sensor, phase separation, humidity-insensitive ionogel,

31 biocompatibility, intra-articular pressure sensing

32

INTRODUCTION

34 A large number of people are suffering from knee joint problems, and severe knee

35 conditions can be benefited from a knee joint surgery [1-3]. Knee joint surgery is a

36 medical procedure aimed at recovering the function of a pathological knee joint and

37 alleviating its pain through surgical intervention, including arthroscopic surgeries,

38 anterior cruciate ligament reconstruction, meniscus repair or removal surgeries, and knee

39 replacement surgeries [4,5]. The World Health Organization (WHO) estimates that

40 millions of people worldwide undergo knee replacement surgery each year [6]. However,

41 about 10%-20% surgical patients accepting the knee joint surgery are dissatisfactory and

42 the dissatisfactory rate continues to increase [7,8], mostly contributed to leg imbalance [9]

43 with an angle deviation >1° and a joint gap <1 mm [10,11]. Real-time monitoring of

44 intra-articular pressure is a promising technology to correct the assemble deviations

45 during knee replacement surgeries for precise alignment of the joints [12,13].

46   The knee joint is curved surfaces bathed in a synovial fluid, and often imposed with

47 high pressure [14,15]. An ideal format for intra-articular pressure sensing should be a soft

48 and thin layer that can be implanted in the narrow and curved gap of the joints (Fig. S1 in

49 the online supplementary file), without being affected by the fluid. Flexible iontronic

50 pressure sensors are a class of emerging devices exhibiting high sensitivity over a wide

51 range [16-21]. Such sensors are often a trilayer with two flexible electrodes sandwiching

52 a soft ionogel, forming a nanoscale electric double layer (EDL) [22,23] at the electrode-

53 ionogel interface (Fig. S2). However, existing iontronic sensors are humidity-sensitive

54 and cannot be used in wet environments because ionogels are often hygroscopic,

55 absorbing water in the air or in humid environments, leading to a dramatic signal-drift of

56 iontronic sensors [24]. On one hand, hydrated ionogels have a substantial change in

57 electrical properties that lead to unstable sensing performance of sensors. On the other

58 hand, mechanical properties of ionogels, such as toughness and modulus, decay in humid

59 conditions. Such a degradation in toughness and modulus causes poor mechanical

60 stability and a narrow working range of sensors. The hygroscopicity of ionogels,

61 therefore, prevents the usage of iontronic pressure sensors as implants for stable pressure

62 measurement during knee replacement surgeries and other in-body applications.

63   Herein, we report a humidity-insensitive, wide-range flexible pressure sensor array for

64 stable intra-articular pressure measurement based on a bicontinuous, non-hygroscopic,

65 and tough ionogel. The ionogel is synthesized in a phase-separation polymerization

66 process that yields two hydrophobic phases: a soft liquid-rich phase and a hard polymer-

67 rich phase. The former provides high ionic conductivity and high ductility, and the latter

68 provides a high Young's modulus (107 MPa) for a wide and linear working range (0-2

69 MPa) for sensing, and both contribute to the humidity-insensitivity. The ionogel also

70 exhibits a high activation energy so that the sensor exhibits high chemical stability over

71 43 years without signal degradation, based on an accelerated aging test. A sensor array

72 with 26 sensors were further implanted in the knee joints in an *in vivo* sheep model, and

73 our sensory system provided real-time and high-precision detection of intra-articular

74 pressure and joint imbalance. This work provides a platform for stable and accurate intra-

75 articular pressure measurement and also for other biomedical applications in wet and

76 high-pressure environments.

77

78 **RESULTS AND DISCUSSION**

79 **Flexible pressure sensors for intra-articular pressure measurement**

80 The knee joint is a curved structure filled with a liquid-like synovial capsule, and often

81 subjected to high pressures. Intra-articular pressure measurements are thus challenging

82 because the implanted sensors in a knee joint should be insusceptible to the curvature,

83 insensitive to humidity, and can detect pressure over a wide range (Fig. 1a). Here, we use

84 a soft iontronic sensor array with a hydrophobic and tough ionogel for humid-insensitive

85 and wide-range intra-articular pressure sensing, and a stretchable bridge-stiff island

86 structure to eliminate the interference of joint curvature. Each sensing unit in the sensor

87 array consists of five layers (Fig. 1b and c): a top polydimethylsiloxane (PDMS)

88 encapsulation layer, a top polyimide-copper (PI-Cu) electrode, an ionogel layer with one

89 side being microstructured, a bottom PI-Cu electrode, and a bottom PDMS encapsulation

90 layer. The electrodes and the ionogel are cut to be rounded with a diameter of 2 mm, with

91 the electrodes connecting to serpentine wires for large stretchability. Each sensor array

92 has 26 sensing units and can be stably laminated on a curved surface (Fig. 1d), while the

93   stretchable bridge-stiffer island structure of the sensor array enables insensitivity to in-

94   plane strain and curvature. The sensors are designed to have the interfaces bonded

95   together to improve the mechanical stability, except for the microstructured interface.

96   Such a seamlessly integrated sensor array can be stretched to 30% without any interlayer

97   delamination or debonding (Fig. 1e). The soft sensor-based technique is substantially

98   different from the traditional method for intra-articular pressure measurement (Fig. S3).

99   Our flexible pressure-assisted monitoring system, in the format of a thin layer that can be

100   filled in the joint, is expected to bypass the need of trial molds, allowing for real-time and

101   accurate pressure monitoring for leg balance during surgery.

102   **Synthesis, mechanical properties, and electrical properties of the ionogel**

103   An ionogel is a composite consisting of a polymer matrix and a ionic liquid in the

104   polymer chains. Ionogels are often hydrophilic because ions are highly polar and

105   hygroscopic. Many nonpolar elastomers, such as PDMS, cannot mix with ionic liquids

106   because of their mismatch in polarity [25]. Here, we *in situ* synthesize a hydrophobic and

107   tough ionogel using acrylonitrile (AN) and ethyl acrylate (EA) as the monomers and 1-

108   ethyl-3-methylimidazolium bis(trifluoromethylsulfonyl)imide ([EMIM][TFSI]) as the

109   ionic liquid. Before polymerization, the AN and EA monomers are all highly miscible

110   with the ionic liquid to form a clear solution. After polymerization, polyethyl acrylate

111   (PEA) and polyacrylonitrile (PAN) have significantly different miscibility with ionic

112   liquids (Fig. S4).

113   PEA is a soft phase that is highly soluble to ionic liquids (Fig. 2a), while polyacrylonitrile

114   (PAN), a highly crystalline polymer (Fig. S5), is almost insoluble to ionic liquids (Fig.

115   2b). As a result, phase separation of PEA and PAN phases occurs in an *in situ*

116   copolymerization process (Fig. 2c). The structure of the P(EA-*co*-AN) ionogel can be

117 tuned by changing the weight ratio of the monomers. The size of the hard phase increases

118 as the content of AN increases from 50 wt.% to 80 wt.% (accordingly, the content of EA

119 decreases from 50 wt.% to 20 wt.%), as illustrated in our transmission electron

120 microscopy (TEM) image (Fig. 2d), as well as the atomic force microscopy-infrared

121 spectroscopy (AFM-IR) observation (Fig. 2e) at a wavenumber of 1570 cm^{-1} (Fig. S6).

122 Furthermore, PEA as an easter, and PAN which contains dense non-polar chains, are both

123 hydrophobic. We show that the P(EA-*co*-AN) ionogel exhibits a water contact angle of

124 99° on a flat surface and 120° on a microstructured surface (Fig. 2f).

125 The coexistence of the hard phase and the soft phase achieves a synergistic

126 enhancement of Young's modulus and tensile strength of the ionogel. The hard PAN

127 phase contributes to the large Young's modulus and strength, while the soft PEA phase

128 contributes to not only ionic conductance, but high toughness of the material because it

129 enhances the stretchability of the material. Both the strength and Young's modulus of the

130 ionogel increase as the content of PAN increases from 50 wt.% to 60 wt.%, with the

131 elongation at break remaining almost unchanged. When the content of PAN increases to

132 80 wt.%, however, the strong dipole interaction [26] between the cyano groups will lead

133 to the formation of defects in the interior. As a result, the material becomes brittle and its

134 toughness decreases substantially (Fig. 2g). We thus select the composition with 60 wt.%

135 PAN for our study because of its high Young's modulus, large stretchability, and high

136 toughness of the ionogel (Fig. 2g). Such properties help achieve a wide sensing range and

137 high robustness of the sensors. Note that our ionogel is even tougher and stiffer than the

138 'ultra-tough and stiff ionogel' of poly(acrylamide-co-acrylic acid) in 1-ethyl-3-

139 methylimidazolium ethyl sulfate [27], single network crosslinked gels [28,29], double-

140 network gels [30,31], solid state ionic conductors [32,33], and other phase separation gels

141 [34,35] (Fig. 2h).

142   In addition to the excellent mechanical properties, the ionogel also exhibits humidity

143 insensitivity. We compared our ionogel with two other ionogels: a poorly hydrophilic

144 copolymer of PEA and polyacrylic acid (P(EA-*co*-AAc)) with ethyl sulfate-1-methyl-3-

145 ethylimidazole (EMIES) as the ionic liquid, and a highly hydrophilic ionogel prepared

146 using acrylamide (AAm) and AAc as monomers, termed (P(AAm-*co*-AAc)), also with

147 EMIES as the ionic liquid. We show that under different relative humidity levels of RH

148 12%, RH 70%, and RH 98% for 30 min, both the Young's modulus and tensile strength

149 of the P(EA-*co*-AN) ionogel remains unchanged (Fig. 2i), while that for the two control

150 ionogels show a substantial decrease in modulus and strength as the relative humidity

151 increase (Fig. S7, S8, and S9). Specifically, at RH 98%, the fracture energies for P(EA-

152 *co*-AAc) and P(AAm-*co*-AAc) decrease by 90.0% and 94.4% compared with the case at

153 RH 12%. Furthermore, the electrical conductivity of the P(EA-*co*-AN) ionogel is also

154 stable under different humidity conditions. By contrast, both control samples, the P(EA-

155 *co*-AAc) and P(AAm-*co*-AAc) ionogels, exhibit a large increase in ionic conductance

156 (Fig. 2j) and capacitance of a capacitor (Fig. S10) in highly humid conditions due to

157 water absorption.

158 **Sensing properties of the sensor array**

159 We used the hydrophobic and tough ionogel as the active layer in a sensor array.

160 Sensitivity, sensing range, and linearity are key parameters of flexible pressure sensors.

161 Sensitivity S is defined as $S=\delta(\Delta C/C_0)/\delta P$, where C represents instantaneous capacitance,

162 C_0 represents the initial capacitance before loading, and P represents applied pressure.

163 We tested the sensitivity of a selected sensing unit in an array under three relative

164   humidity levels (RH 12%, RH 70% and RH 98%). The results show that the sensing units

165   exhibit constant and close sensitivity values of 2.43, 2.47, and 2.48 kPa^{-1} (Fig. 3a), all

166   with high linearity (R^2>0.998) in a wide range of 0-2.0 MPa. The wide range and linear

167   response is related to both the structure design and the large Young's modulus of the

168   ionogel. The microstructure, a pillar-like structure with synergetic gradients in the width

169   and height directions, is developed using a machine learning model for a linear response

170   [36]. The linear range is further widened by using the ionogel with a large Young's

171   modulus, although there is often a trade-off between linear range and sensitivity (Fig.

172   S11).

173   Both the angular resolution and pressure resolution are important for intra-articular

174   pressure sensing applications. Angular resolution is defined as the minimal rotational

175   change of angle that the array can resolve. We built a setup to detect the angular

176   resolution by imposing a force to an artificial femur to press a sensor array and change its

177   inter-axis angle with an increment of 0.1° at the initial angle of 90° (Fig. 3b). We show

178   that the rotation can be detected from a selected pixel in the array, indicating an angular

179   resolution of at least 0.1° (Fig. 3c). Besides, the limit of detection of the sensor array is

180   determined to be 0.38 Pa, and the pressure-resolution at preloads of 100, 500, and 1000

181   kPa are determined to be 32 Pa, 422 Pa, and 1.55 kPa, respectively (Fig. 3d). Such high

182   angular resolution and pressure-resolution enable precise measurement of intro-articular

183   pressure of our sensor array.

184   The sensing properties of the sensing units are highly uniform. We tested all 26 pixels

185   in an array and the results show a small sensitivity difference of only 0.8%, with all

186   sensing units exhibiting high linearity (R^2>0.998) (Fig. 3e). The deviation is even smaller

187   than that of commercial silicon-based MEMS sensors [37,38]. The high uniformity stems

188   from the contact mode of iontronic sensing—the signal magnitude is determined by the

189   interfacial contact area rather than the thickness of the ionogel [39]. A small difference in

190   thickness of the ionogel will not affect the response of the iontronic sensor. By contrast,

191   the signal magnitude of conventional capacitive sensors highly relies on the thickness

192   control of the dielectric layer, for which the deviation is difficult to control.

193   **Conformability and strain-insensitivity of the flexible pressure sensor array**

194   Serpentine interconnects have been proven to be effective to achieve large stretchability

195   and conformability of electronic devices [40-42]. Here, the sensor array was designed to

196   have a stretchable bridge stiff-island structure [43]. The islands are sensing units of a

197   rigid PI-Cu/ionogel/PI-Cu trilayer, with all materials being bendable but the trilayer being

198   not stretchable (Fig. 3f). The bridges are flexible and stretchable serpentine interconnects,

199   encapsulated by a PDMS layer. Upon stretching, only the serpentines and the PDMS

200   encapsulation layers are elongated, while negligible deformation of the sensing units

201   occurs. Such a structure helps eliminate the response of the sensing units to in-plane

202   strains. We show that the capacitance-pressure response of a sensing unit does not change

203   when it is stretched from 0 to 20%, and no signal is detected when the sensor array is

204   subjected to in-plane strains or covered on a curved surface, including the curved surface

205   of a joint (Fig. 3g).

206   **Mechanical and chemical stability of the sensor array**

207   The mechanical stability of the sensor array should also be considered since the knee

208   joints are often subjected to both high shear stress and high pressure. We use interfacial

209   bonding to improve the mechanical stability of the sensor array (Fig. 3h). Specifically, a

210   monolayer of 3-mercaptopropyl-triethoxysilane (MPTMS) containing a mercapto group

211 and a monolayer of 3-(trime-thoxysilyl)propyl methacrylate (TMSPMA) containing an

212 unsaturated double bond were used to modify the surface of the Au coated PI-Cu

213 electrode (Fig. S12). The Au layer and the thiol groups of the MPTMS monolayer form

214 strong Au-S interaction [44,45], and the two monolayers are bonded via a condensation

215 reaction. The unsaturated double bonds of TMSPMA are exposed, which build a strong

216 bond with the C=C bond in EA and AN monomers during the photo-polymerization

217 process. Besides the adhesion between the ionogel and the Cu electrode, the two PDMS

218 encapsulation layers are plasma-treated and bonded via the formation Si-O-Si covalent

219 bonds for sealing [46,47]. Such modification greatly improves the mechanical stability of

220 the interfaces: the interfacial toughness between the flat surface of the ionogel and the

221 electrode is as high as 418 $J \cdot m^{-2}$. Without chemical bonding, the interfacial toughness is

222 only 22 $J \cdot m^{-2}$. In addition, the interfacial toughness of the PDMS-PDMS encapsulation

223 layers is 369 $J \cdot m^{-2}$ (Fig. 3i), which is otherwise only ~1.3 $J \cdot m^{-2}$ without interfacial

224 bonding.

225 We further explored the fatigue resistance of the sensor array when it is used under

226 high shear and pressure conditions. We randomly select a sensing unit in an array for the

227 cyclic friction test. The results show that the sensor can stably work over 2,000 cycles

228 under a combined high pressure of 1.0 MPa and a shear stress of 220 kPa, without

229 exhibiting signal drift (Fig. 3j) or interfacial failure (Fig. 3k). By contrast, a control

230 sensor , for which all interlayers are simply stacked without bonding, shows substantial

231 signal drift under combined compression and shear. Delamination between the functional

232 layers is also found (Fig. S13).

233   The sensors are chemically stable over tens of years under a normal working condition.

234   We performed an accelerated aging test of the sensor array under a humidity-heat aging

235   condition (at RH 98% and 328 K), and also tested the degradation activation energy of

236   the ionogel (E_a) using a thermogravimetric analyzer (Fig. S14). The activation energy

237   was determined to be 0.80 eV from the derivative curves of different heating rates and its

238   mass loss, corresponding to an acceleration factor (AF) of 131 based on the Hallberg-

239   Peck model [48,49]. We tested the responses of four sensors in a sensing array under

240   different aging times and found that the responses do not change over 120 days in the

241   aging condition, corresponding to 43 years under a normal working condition of RH 50%

242   and 298 K (Fig. 3l).

243   **Biocompatibility of the sensor array**

244   The biocompatibility of the sensor array has been studied to confirm its potential

245   applications in joints. We evaluate the biocompatibility by conducting *in vitro*

246   cytotoxicity, acute toxicity, and pyrogen tests, as well as *in vivo* inflammation test

247   through histological observation. The *in vitro* cytotoxicity test was conducted by extract

248   injection or by subcutaneous implantation (Fig. 4a), and a pressure sensor array were

249   used for test sample extract. First, L-929 cells were digested using trypsin with a cell

250   suspension of 1×10^5 cells per milliliter and then cultured in an incubator at minimum

251   essential medium (MEM) with 10% fetal bovine serum. After the cells grow into a

252   monolayer, the original culture medium was aspirated, and 100 ml of test sample extracts

253   (concentrations of 100%, 75%, 50%, 25%), blank control solution, positive control

254   solution, and negative control solution to further culture at 37°C in 5% CO_2 for 24 h.

255   After culturing, the cell morphology was observed by fluorescence microscopy, and its

256   absorbance at 570 nm was measured (reference wavelength: 650 nm) on a microplate

257 reader to observe the cell survival rate. The results show that the survival rates are all

258 higher than 87.6%, indicating that the sensor array has no significant toxicity to L-929

259 cells (Fig. 4b).

260   Acute toxicity was also tested by injecting the test sample extract and negative control

261 solution. The selected extraction solvent is 0.9 wt.% sodium chloride injection, and the

262 extraction ratio is 3 cm^2 per milliliter, and the injection dose is 50 ml kg^{-1}. No significant

263 difference in weight between the experimental animal and the control animal was

264 observed, indicating that the polar extract of the test sample does not cause acute toxicity

265 (Fig. 4c). A similar operation of injecting extract was used to do the pyrogen test and

266 there was no temperature difference between the experimental and the control animals

267 (Fig. 4d). The results are in accordance with the pyrogen test regulations.

268   We further used hematoxylin-eosin staining to evaluate inflammation by subcutaneous

269 implantation of a sensor array in a mouse model by a blinded pathologist. Histological

270 assessment shows that both the control sample and the experimental sample have mild

271 inflammatory cell infiltration after 1 week. The degree of inflammation at the

272 implantation site with the control sample and with the sensor array receives an average

273 score of 0.5 and 1, respectively, all falling in the 'very mild' inflammation range (Fig.

274 4e). The result is satisfactory for a short period of implantation in joints.

275 ***In vitro* pressure measurement of the sensor array in a knee model**

276 We used the sensor array for pressure measurement in an *in vitro* prosthetic knee model

277 (Fig. 4f). A pressure sensor array was placed in the joint of a prosthetic knee model and

278 the signal of each channel was recorded when a force was applied (Fig. 4g and h). Under

279 applied normal forces of 10 and 40 N, the measured force (F_M, by summing signals from

280 all channels) is compared with the applied force (F_a). F_m can be figured out by Equation

281 (1):

$$F_m = \sum_{i=1}^{26} P_i \cdot A \qquad (1)$$

282 where P_i is the pressure value of each pixel that can be measured by sensor number i (as

283 shown in Fig. 3e), and A is the area of a single pixel. The pressure is applied only to the

284 sensing areas rather than the gaps between the sensors (Fig. S15). F_m was found to match

285 well with F_a in both cases (Fig. 4i). The results show that the sensor array can accurately

286 measure the load applied to the joint.

287 **Real-time and *in vivo* intra-articular pressure recording**

288 We further constructed an intra-articular pressure measurement system (Fig. 5a) for real-

289 time and *in vivo* pressure recording since our sensor array presents high compatibility and

290 accuracy. The intra-articular pressure measurement system contains two sensor arrays for

291 the lateral condyle and medial condyle (Fig. 5b), respectively, together with their

292 companying read-out circuit (Fig. 5c). The read-out circuit uses a method called

293 'frequency division multiplexing' for signal readout—each sensing unit is read using a

294 separate and encoded frequency to avoid interpixel interference and crosstalk, given that

295 the response of iontronic sensors is frequency dependent [50]. The orthogonal frequency

296 is propagated to the decoder using a capacitor-voltage converter, and the real-time,

297 crosstalk-free signal acquisition of the sensor array is realized using a field programmable

298 gate array (Fig. S16).

299 The sensor arrays were sutured on the tibia surface (Fig. S17) of a sheep model using

300 bone screws by a surgeon for pressure recording (Fig. 5d). The temperature during

301 implantation is consistent with that of the animal model, approximately 38.5 °C.

302 Furthermore, the sensor is fully submerged in a synovial fluid, making humidity-

303 insensitivity essential to ensure its reliability in such an environment. We slowly rotated

304 the femur from the lateral to the medial condyle side in an angular range of –5° to +5° to

305 record the real-time intra-articular pressure during the rotation, and we show that the

306 signals from the two sensor arrays all changes with the rotational angle, with the signal

307 amplitudes of the two arrays being supplementary (Fig. 5e). We further define a

308 coordinate system for the knee joint, with x-axis situating along the two articular fossa, y-

309 axis situating along the articular surface and perpendicular to the x-axis, and z-axis being

310 perpendicular to both the x- and y-axis. The interaxial angles of the tibial orientation are

311 defined as θ_1 in the x-y plane and θ_2 in the x-z plane (Fig. 5f). We tested the real-time

312 pressure distribution of nine combined states with θ_1 of –5°, 0, and +5°, and θ_2 of 0, 45°,

313 and 90° by rotating the femur (Fig. S18). Our system can visually display the real-time

314 pressure distribution of the nine states, and the results show that the pressure is not

315 uniformly distributed on the joint surfaces but rather concentrated. Furthermore, the tilt

316 angle significantly affects the balance of the lateral and medial condyles, and thus our

317 system can be potentially used to provide visual information for imbalance correction.

318 We expect that our real-time pressure measurement system can be used for unbalanced

319 pressure correction in not only knee joins, but also many other articular joints.

320

321 **MATERIALS AND METHODS**

322 Detailed materials and methods are available in the Supplementary data.

323

324 **SUPPLEMENTARY DATA**

325 Supplementary data are available at *NSR* online.

326 **FUNDING**

332 **AUTHOR CONTRIBUTIONS**

333 C.F.G. conceived the idea and designed the research. S.X. and J.S. performed the

334 majority of the experiments. Z.L. and M.C. printed the microstructured template for the

335 ionogels. S.X. and J.S. drafted the manuscript, and C.F.G. revised the manuscript.

336 *Conflict of interest statement.* None declared.

337

338 **REFERENCES**

339 1. Evans JT Whitehouse MR. Partial versus total knee replacement for knee

340   osteoarthritis. *The Lancet* 2019; **394**: 712–3.

341 2. Duong V, Oo WM, Ding C *et al*. Evaluation and treatment of knee pain: a review.

342   *JAMA* 2023; **330**: 1568–80.

343 3. Saul H, Cassidy S, Deeney B *et al*. Routine follow-up may not be needed for people

344   undergoing joint replacement surgery. *BMJ* 2023; **380**: 222.

345 4. Katz JN, Arant KR, Loeser RF. Diagnosis and treatment of hip and knee

346   osteoarthritis: a review. *JAMA* 2021; **325**: 568–78.

347   5. Martel-Pelletier J, Barr AJ, Cicuttini FM *et al*. Osteoarthritis. *Nat Rev Dis Primers*

348   2016; **2**: 16072.

349   6. Price AJ, Alvand A, Troelsen A *et al*. Knee replacement. *The Lancet* 2018; **392**:

350   1672–82.

351   7. Liddle AD, Judge A, Pandit H *et al*. Adverse outcomes after total and

352   unicompartmental knee replacement in 101 330 matched patients: a study of data

353   from the National Joint Registry for England and Wales. *The Lancet* 2014; **384**:

354   1437–45.

355   8. Buhagiar MA, Naylor JM, Harris IA *et al*. Effect of inpatient rehabilitation vs a

356   monitored home-based program on mobility in patients with total knee arthroplasty:

357   the HIHO randomized clinical trial. *JAMA* 2017; **317**: 1037–46.

358   9. Gu Y, Howell SM, Hull ML. Simulation of total knee arthroplasty in 5 or 7 valgus: a

359   study of gap imbalances and changes in limb and knee alignments from native. *J*

360   *Orthop Res* 2017; **35**: 2031–39.

361   10. Matziolis G, Brodt S, Windisch C *et al*. The reversed gap technique produces

362   anatomical alignment with less midflexion instability in total knee arthroplasty: a

363   prospective randomized trial. *Knee Surg Sports Traumatol Arthrosc* 2016; **24**: 2430–

364   35.

365   11. Longo UG, Candela V, Pirato F *et al*. Midflexion instability in total knee arthroplasty:

366   a systematic review. *Knee Surg Sports Traumatol Arthrosc* 2021; **29**: 370–38.

367   12. Gustke KA, Golladay GJ, Roche MW *et al*. Increased satisfaction after total knee

368   replacement using sensor-guided technology. *Bone Joint J* 2014; **96**: 1333–38.

369   13. Wu L, Xue J, Meng J *et al*. Self-powered flexible sensor array for dynamic pressure

370   monitoring. *Adv Funct Mater* 2024; **8**: 2316712 .

371   14. Lin W, Klein J. Recent progress in cartilage lubrication. *Adv Mater* 2021; **33**:

372   2005513.

373   15. Paital SR, Dahotre NB. Calcium phosphate coatings for bio-implant applications:

374   Materials, performance factors, and methodologies. *Mater Sci Eng R Rep* 2009; **66**: 1-

375   70.

376   16. Ji B, Zhou Q, Hu B *et al*. Bio-inspired hybrid dielectric for capacitive and

377   triboelectric tactile sensors with high sensitivity and ultrawide linearity range. *Adv*

378   *Mater* 2021; **33**: 2100859.

379   17. Shi J,Dai Y, Cheng Y *et al*. Embedment of sensing elements for robust, highly

380   sensitive, and cross-talk–free iontronic skins for robotics applications. *Sci Adv 2*023;

381   **9**: eadf8831.

382   18. Lu P, Wang L, Zhu P *et al*. Iontronic pressure sensor with high sensitivity and linear

383   response over a wide pressure range based on soft micropillared electrodes. *Sci Bull*

384   2021; **66:** 1091–1100.

385   19. Shen Z, Zhu X, Majidi C *et al*. Cutaneous ionogel mechanoreceptors for soft

386   machines, physiological sensing, and amputee prostheses. *Adv Mater* 2021; **33**:

387   2102069.

388   20. Gu G, Zhang N, Xu H *et al*. A soft neuroprosthetic hand providing simultaneous

389   myoelectric control and tactile feedback. *Nat Biomed Eng* 2023; **7**: 589-98.

390   21. Xu H, Chai G, Zhang N *et al*. Restoring finger-specific tactile sensations with a

391   sensory soft neuroprosthetic hand through electrotactile stimulation. *Soft Sci* 2022;

392   **2**:19.

393   22. Bai N, Wang L, Wang Q *et al*. Graded intrafillable architecture-based iontronic
394   pressure sensor with ultra-broad-range high sensitivity. *Nat Commun* 2020; **11**: 209.

395   23. Cheng Y, Zhan Y, Guan F *et al*. Displacement-pressure biparametrically regulated
396   softness sensory system for intraocular pressure monitoring. *Natl Sci Rev* 2024; 11:
397   nwae050.

398   24. Esteves C, Palam SICJ, Costa HMA *et al*. Tackling humidity with designer ionic
399   liquid-based gas sensing soft materials. *Adv Mater* 2022; **34**: 2107205.

400   25. Ueno K, Fukai T, Nagatsuka T *et al*. Solubility of poly (methyl methacrylate) in ionic
401   liquids in relation to solvent parameters. *Langmuir* 2014; **30**: 3228-35.

402   26. Fu R, Guan Y, Xiao C *et al*. Tough and highly efficient underwater self-repairing
403   hydrogels for soft electronics. *Small Methods* 2022; **6**: 2101513.

404   27. Wang M,Zhang P, Shamsi M *et al.* Tough and stretchable ionogels by in situ phase
405   separation. *Nat Mater* 2022; **21**: 359–65.

406   28. Li B, Xu F, Guan T *et al*. Self-adhesive self-healing thermochromic ionogels for
407   smart windows with excellent environmental and mechanical stability, solar
408   modulation, and antifogging capabilities. *Adv Mater* 2023; **35**: 2211456.

409   29. Kim JH, Cho KG, Cho DH *et al*. Ultra-sensitive and stretchable ionic skins for high-
410   precision motion monitoring. *Adv Funct Mater* 2021; **31**: 2010199.

411   30. Xuan HD, Timothy B, Park H-Y *et al*. Super stretchable and durable
412   electroluminescent devices based on double-network ionogels. *Adv Mater* 2021; **33**:
413   2008849.

414   31. Kamio E, Yasui T, Iida Y *et al*. Inorganic/organic double-network gels containing
415   ionic liquids. *Adv Mater* 2017; **29**: 1704118.

416   32. Charaya H, Li X, Jen N *et al*. Specific ion effects in polyampholyte hydrogels

417   dialyzed in aqueous electrolytic solutions. *Langmuir* 2018; **35**: 1526–33.

418   33. He Y, Cheng Y, Yang C *et al*. Creep-free polyelectrolyte elastomer for drift-free

419   iontronic sensing. *Nat Mater* 2024; **4**: https://doi.org/10.1038/s41563-024-01848-6.

420   34. Zhao W, Zheng Y, Huang A *et al*. Metal-halogen interactions inducing phase

421   separation for self-healing and tough ionogels with tunable thermoelectric

422   performance. *Adv Mater* 2024; **2**: 2402386.

423   35. Tie J, Mao Z, Zhang L *et al*. Strong and ultratough ionogel enabled by ingenious

424   combined ionic liquids induced microphase separation. *Adv Funct Mater* 2023; **33**:

425   2307367.

426   36. Liu Z, Cai M, Hong S *et al*. Data-driven inverse design of flexible pressure sensors.

427   *Proc Natl Acad Sci USA* 2024; **28**: e2320222121.

428   37. Chi C, Sun Xu, Li T *et al*. A flexible tactile sensor with good consistency. *IEEE*

429   *Access* 2018; **6**: 51647–54.

430   38. Shang X., Wang N, Cao S *et al*. Fiber-integrated force sensor using 3D printed

431   spring-composed fabry-perot cavities with a high precision down to tens of

432   piconewton. *Adv Mater* 2024; **36**: 2305121.

433   39. Chang Y, Wang L, Li R *et al*. First decade of interfacial iontronic sensing: from

434   droplet sensors to artificial skins. *Adv Mater* 2021; **33**: 2003464.

435   40. Rao Z, Lu Y, Li Z *et al*. Curvy, shape-adaptive imagers based on printed

436   optoelectronic pixels with a kirigami design. *Nat Electron* 2021; **4**, 513–21.

437   41. Yong K, De S, Hsieh ET *et al*. Kirigami-inspired strain-insensitive sensors based on

438   atomically-thin materials. *Mater Today* 2020; **34**: 58–65.

439   42. Zhang M, Sun JJ, Khatib M *et al*. Time-space-resolved origami hierarchical

440   electronics for ultrasensitive detection of physical and chemical stimuli. *Nat Commun*

441   2019; **10**: 1120.

442   43. Kim D-H, Song J, Choi WM *et al*. Materials and noncoplanar mesh designs for

443   integrated circuits with linear elastic responses to extreme mechanical deformations.

444   *Proc Natl Acad Sci USA* 2008; **105**: 18675–80.

445   44. Inkpen MS, Liu Z-F, Li H *et al*. Non-chemisorbed gold–sulfur binding prevails in

446   self-assembled monolayers. *Nat Chem* 2019; **11**: 351–8.

447   45. Reimers JR, Ford MJ, Marcuccio SM *et al*. Competition of van der Waals and

448   chemical forces on gold–sulfur surfaces and nanoparticles. *Nat Rev Chem* 2017; **1**:

449   0017.

450   46. Hollahan JR, Carlson GL. Hydroxylation of polymethylsiloxane surfaces by

451   oxidizing plasmas. *J Appl Polym Sci* 1970; **14**: 2499–508.

452   47. Owen MJ, Smith PJ. Plasma treatment of polydimethylsiloxane. *J Adhes Sci Technol*

453   1994; **8**: 1063–75.

454   48. Gao Z, Yin X, Zhang B *et al*. A Wiener process–based remaining life prediction

455   method for light-emitting diode driving power in rail vehicle carriage. *Adv Mech Eng*

456   2019; **11**: 1687814019832215.

457   49. Wang L, Li Z, Cao C *et al*. Facile and dynamic infrared modulation of durable

458   VO$_2$/CuI films for smart window applications. *Chem Eng J* 2024; **488**: 150972.

459   50. Li Z, Yang J, Zhang Y *et al*. Ultrafast readout, crosstalk suppression iontronic array

460   enabled by frequency-coding architecture. *npj Flex Electron* 2024; **8**: 9.

461

462
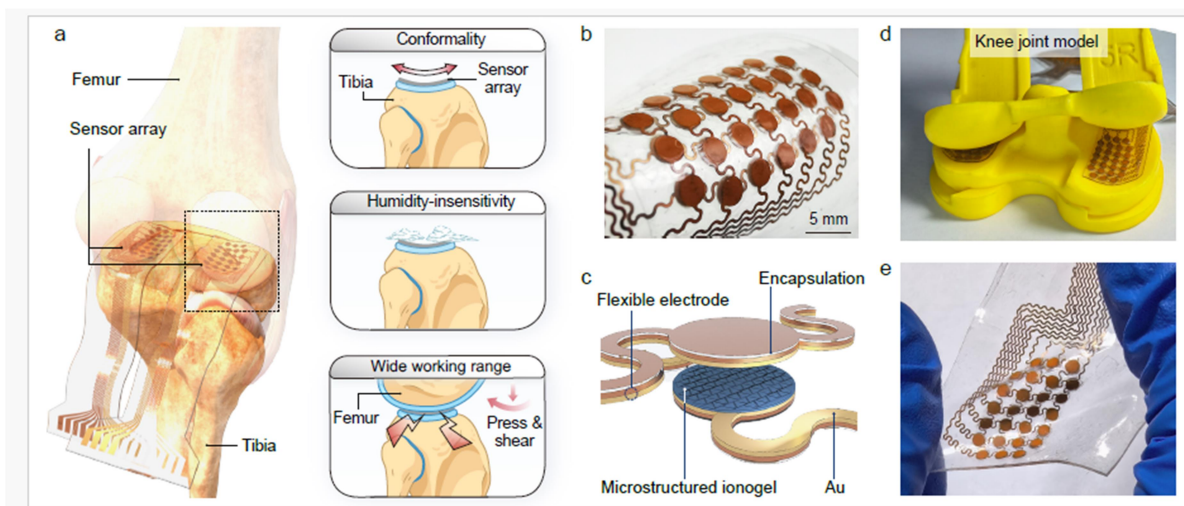
Figure 1. Challenges for intra-articular pressure measurement, and flexible iontronic pressure sensor array used in the measurement. (a) Conditions required for intra-articular pressure measurement: sensing on a curved surface, in highly-humid condition, and under high pressure and shear. (b) P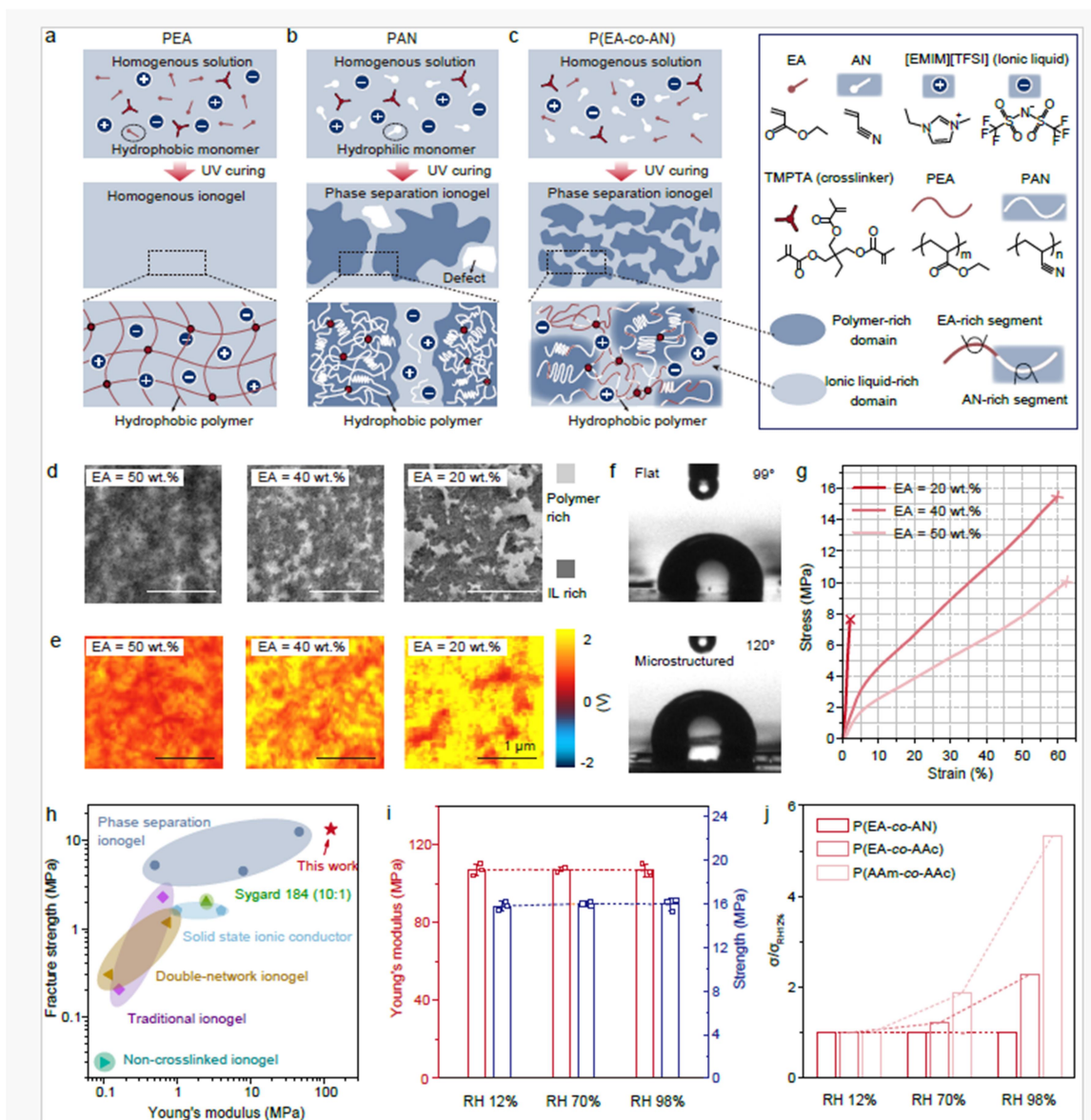hotographs of the flexible iontronic pressure sensing array. (c) Schematic showing the structure of the sensor array. (d) The flexible iontronic pressure sensor array can be laminated on curved surfaces of a knee joint model. (e) Photograph of the flexible iontronic pressure sensor array when stretched to 30%.

472

473

Figure 2. Preparation, mechanical properties, and electrical properties of ionogels under different relative humidity levels. (a) Polymerization of single-phased PEA ionogel. (b) Polymerization of the PAN ionogel, which often has internal defects. (c) Phase separation of P(EA-*co*-AN) ionogel. (d) TEM images of P(EA-*co*-AN) ionogels with EA contents of 50 wt.%, 40 wt.%, and 20 wt.%. (e) AFM-IR images of P(EA-*co*-AN) ionogels with EA

479 contents of 50 wt.%, 40 wt.%, and 20 wt.%. (f) Water contact angles of P(EA-*co*-AN)

480 ionogel on a flat surface and a microstructured surface, showing the hydrophobic nature

481 of the material. (g) Tensile stress-strain curves of the ionogels with different monomer

482 ratios. (h) Comparison of modulus and tensile strength between our ionogel and the

483 reported results of other ionogels [27-35]. (i) Modulus and tensile strength of the ionogel

484 in different relative humidity levels of RH 12%, RH 70%, and RH 98%. (j) Ionic

485 conductivity of our ionogel in reference to that at RH 12% and that of the two control

486 samples, P(EA-*co*-AAc) and P(AAm-*co*-AAc), in different relative humidity levels.

487

488

489
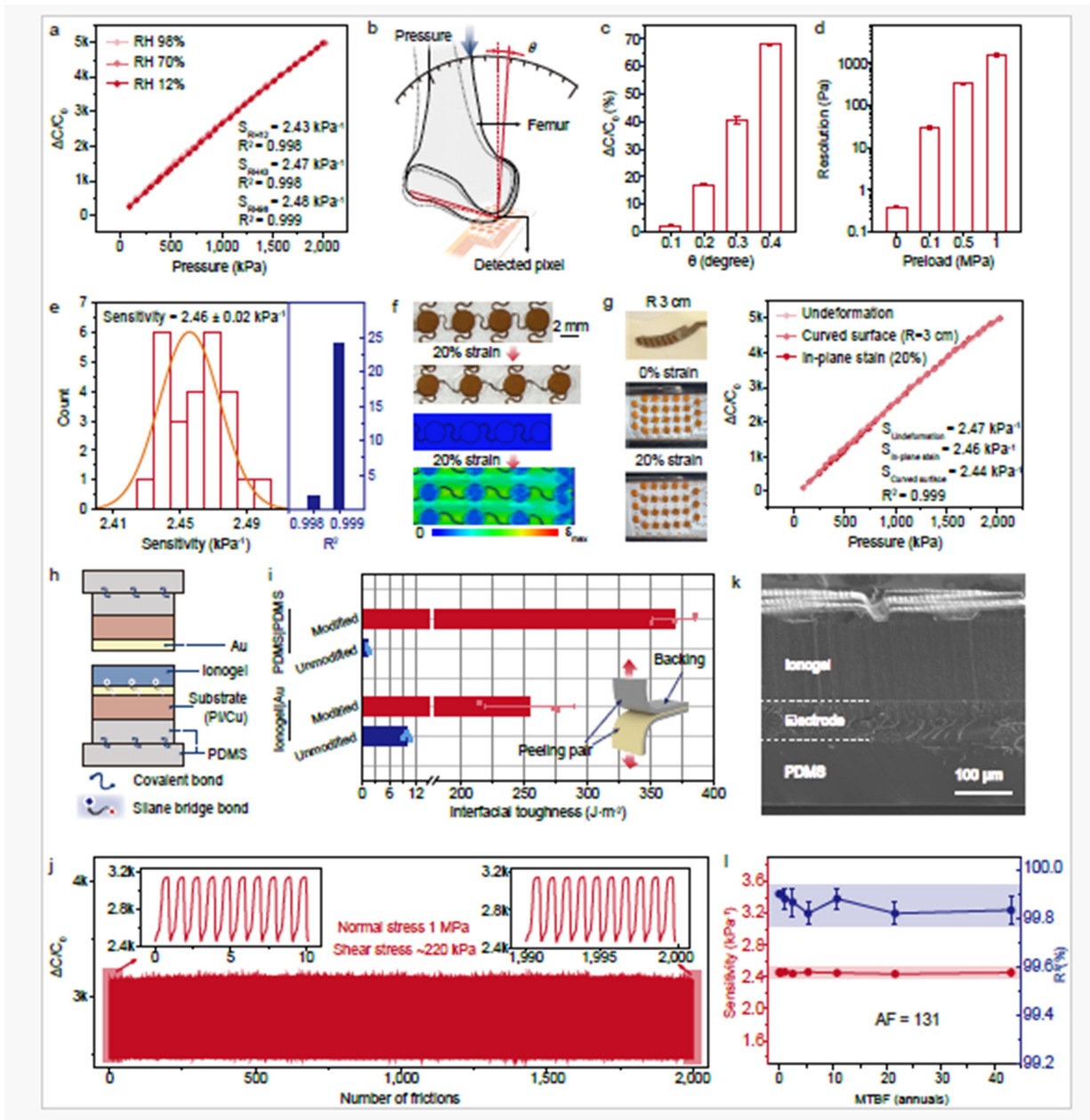
Figure 3. Sensing properties and stability of the flexible iontronic pressure sensor array. (a) Response curves of a single sensing unit under different relative humidity levels of RH 12%, 70%, and 98%. (b) Schematic diagram of the setup for the test of angular resolution. (c) Response of the sensor to angular changes of 0.1°, 0.2°, 0.3°, and 0.4°. An

494   angular resolution of at least 0.1° is determined. (d) Pressure-resolutions of the sensor

495   under different preloads of 0, 0.1, 0.5, and 1.0 MPa. (e) Statistic distribution of sensitivity

496   and linearity values of 26 pixels in a sensor array. (f) Photographs and simulation results

497   of a sensor array stretched from 0 to 20%. (g) Capacitance-pressure responses of a single

498   sensing unit under no in-plane strain, subjected to in-plane strain of 20%, and laminated

499   on a curved surface, showing that the response is insensitive to in-plane strain or

500   curvature. (h) Schematic of the layered structure of the sensor. (i) Interfacial toughness of

501   the covalently bonded interfaces in panel (h). Without interfacial bonding, the interfacial

502   adhesion is much poor. (j) Response of a sensing unit under repeated rubbing of 2,000

503   cycles. The applied pressure is 1 MPa, and the shear stress is 220 kPa. (k) Cross-sectional

504   view SEM image of the sensor after rubbing test. No delamination between the interfaces

505   is observed. (l) Sensitivity and linearity over mean time between failure (MTBF) of a

506   sensing unit measured in an accelerated aging test. The acceleration factor (AF) is 131.

507   Both sensitivity and linearity maintain almost unchanged over the test (43 annuals).

508
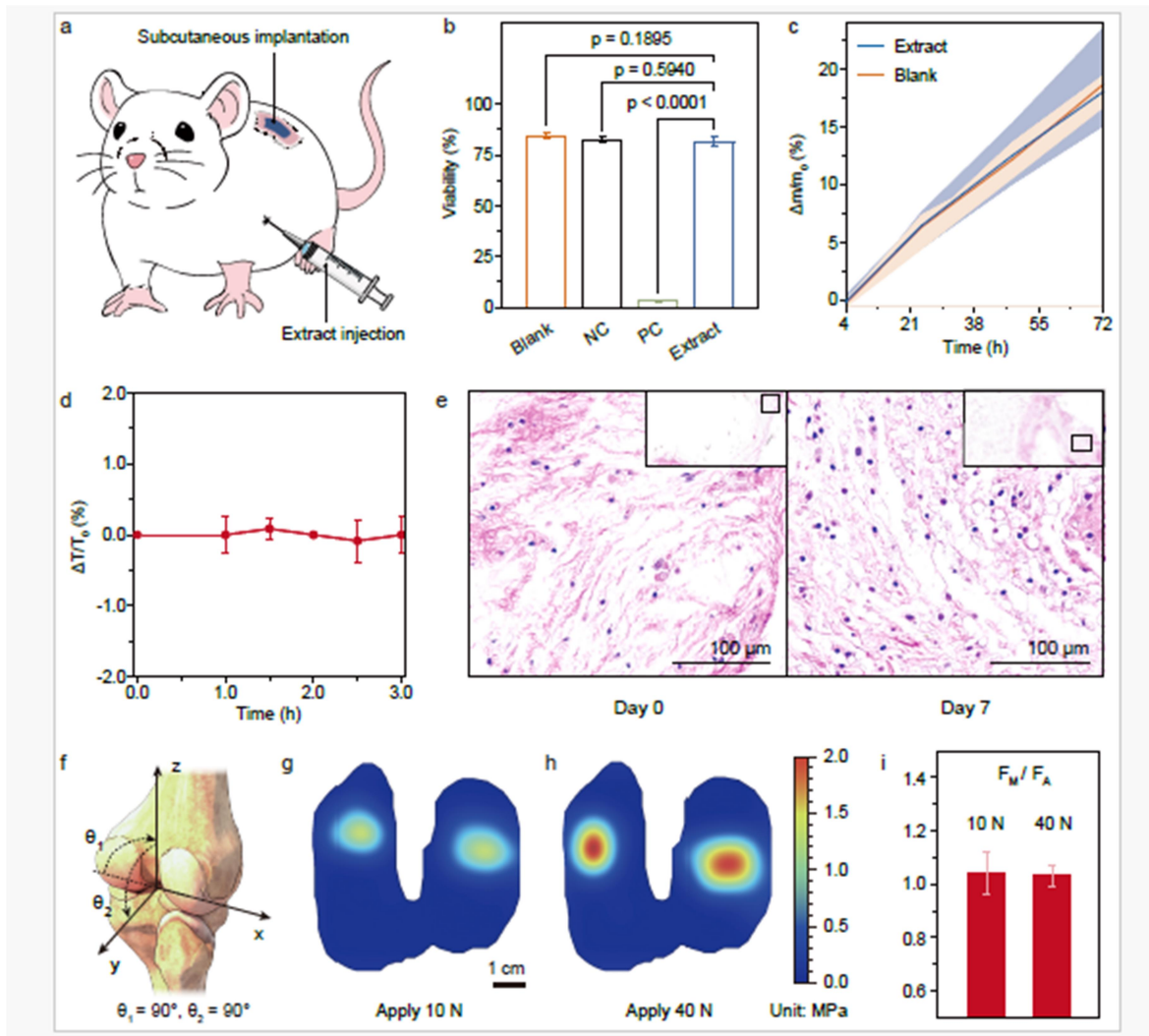
Figure 4. Cytotoxicity, *in vivo* biocompatibility of the sensor array, and its validity for pressure measurement in a knee joint model. (a) Schematic diagram of the *in vitro* and *in vivo* biocompatibility test using extract injection or the subcutaneous implantation in a mouse model. (b) *In vitro* cytotoxicity test of the sensor array. Results from blank control, negative control (NC), and positive control (PC) groups are compared. The survival rates are all higher than 87.6%, indicating that the sensor array has no significant toxicity. (c) Mass change of a mouse injected with a sensor array extract in an acute

518   systemic toxicity test with its error range. The result is close to that of the control model

519   without the extract injection. Δm is the change in mass, and m_0 is the original mass before

520   the test. (d) Temperature change of a mouse for a pyrogen test, where ΔT is the change in

521   temperature, and T_0 is the original temperature before the test. (e) *In vivo*

522   biocompatibility test of the arrays by histological observation of tissue slices after

523   implanting for 7 d. (f) Schematic diagram of an *in vitro* bone model for intra-articular

524   pressure test. (g) The pressure mapping of the tibia plane with 10 N vertical stress and (h)

525   40 N vertical stress. (i) Ratios of measured force to applied force under loads of 10 N and

526   40 N. Both values are close to 1.0.

527

528

529
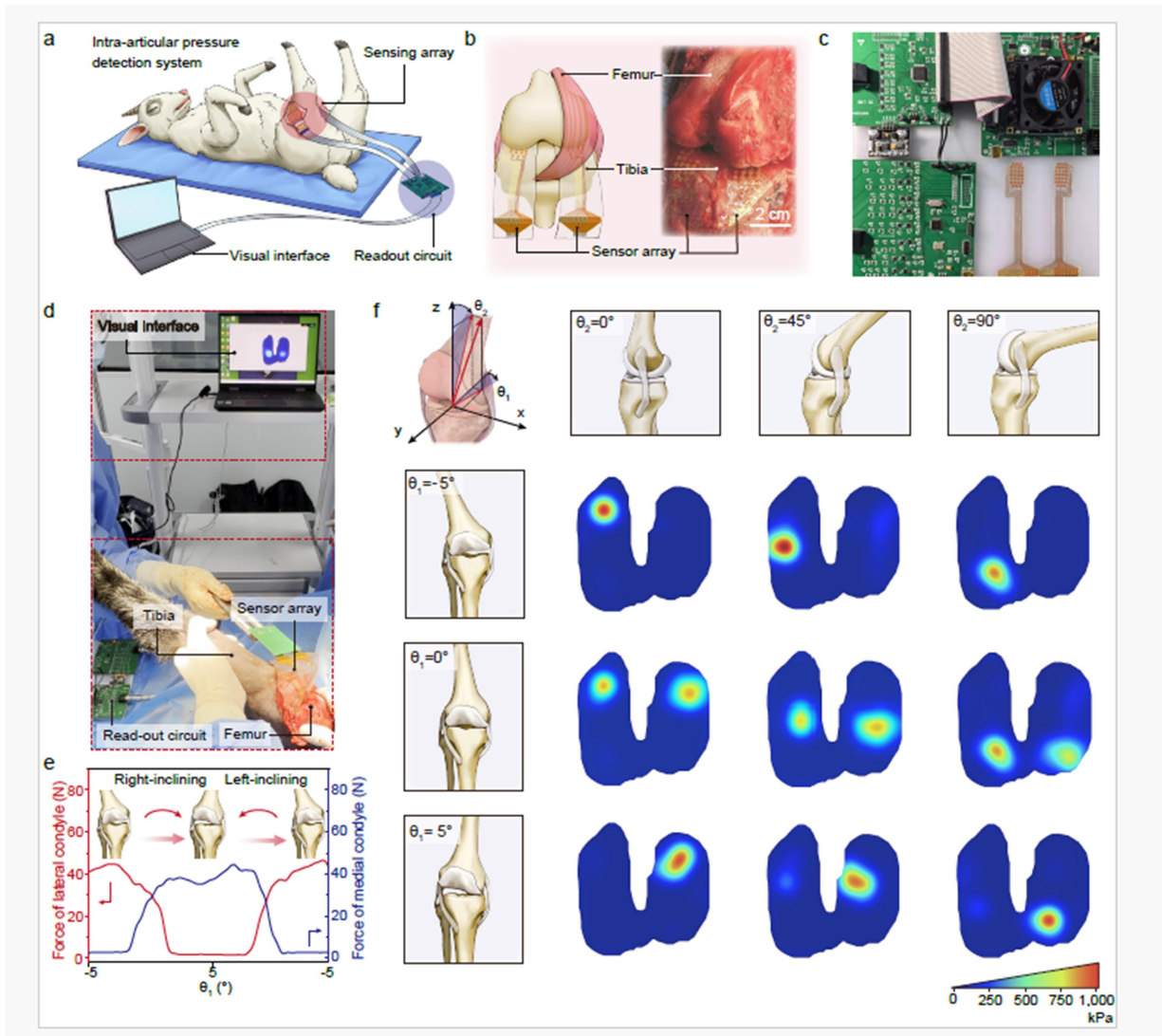
Figure 5. *In vivo* intra-articular pressure detection in a sheep model using flexible iontronic pressure sensor arrays. (a) Schematic diagram of intra-articular pressure detection using a sensory system in a sheep model. The sensory system includes two sensor arrays, a circuit, and a computer with real-time visual interface showing pressure distribution. (b) Schematic and photograph for the implantation of two sensory arrays between the femur and the tibia of a knee joint. (c) Photograph of the readout circuit. (d) Photograph of the *in vivo* intra-pressure measurement of a knee joint in a sheep model.

537   (e) Detected force of the lateral and medial condyles when rotating the tibia from –5° to

538   +5°. (f) Intra-articular pressure mapping of nine states when the femur changes from the

539   extension position (θ_2=0°) to the middle position (θ_2=45°) and to the flexion position

540   (θ_2=90°), and angel θ_1 changes from –5° to 0, and to +5°.

541